HHS Public Access

Author manuscript

Magn Reson Med. Author manuscript; available in PMC 2022 January 01.

Published in final edited form as:

Magn Reson Med. 2021 January ; 85(1): 390–403. doi:10.1002/mrm.28419.

Probing *in vivo* cortical myeloarchitecture in humans via line-scan diffusion acquisitions at 7T with 250–500 micron radial resolution

Mukund Balasubramanian[*,1,2], **Robert V. Mulkern**[1,2], **Jeffrey J. Neil**[3], **Stephan E. Maier**[1,4,5], **Jonathan R. Polimeni**[1,6,7]

[1]Harvard Medical School, Boston, MA, USA

[2]Department of Radiology, Boston Children's Hospital, Boston, MA, USA

[3]Department of Neurology, Washington University School of Medicine, Saint Louis, MO, USA

[4]Department of Radiology, Brigham and Women's Hospital, Boston, MA, USA

[5]Institute of Clinical Sciences, Sahlgrenska University Hospital, Gothenburg, Sweden

[6]Athinoula A. Martinos Center for Biomedical Imaging, Department of Radiology, Massachusetts General Hospital, Charlestown, MA, USA

[7]Harvard-MIT Division of Health Sciences and Technology, Massachusetts Institute of Technology, Cambridge, MA, USA

Abstract

Purpose: The goal of this study was to measure diffusion signals within cerebral cortex using the line-scan technique to achieve extremely high resolution in the radial direction (i.e., perpendicular to the cortical surface) and to demonstrate the utility of these measurements for investigating laminar architecture in the living human brain.

Methods: Line-scan diffusion data with 250–500 micron radial resolution were acquired at 7T on eight healthy volunteers, with each line prescribed perpendicularly to primary somatosensory cortex (S1) and primary motor cortex (M1). Apparent diffusion coefficients (ADCs), fractional anisotropy (FA) values and radiality indices were measured as a function of cortical depth.

Results: In the deep layers of S1, we found evidence for high anisotropy and predominantly tangential diffusion, with low anisotropy observed in superficial S1. In M1, moderate anisotropy and predominantly radial diffusion was seen at almost all cortical depths. These patterns were consistent across subjects and were conspicuous without averaging data across different locations on the cortical sheet.

Conclusion: Our results are in accord with the myeloarchitecture of S1 and M1, known from prior histology studies: in S1, dense bands of tangential myelinated fibers run through the deep layers but not the superficial ones, and in M1, radial myelinated fibers are prominent at most cortical depths. This work therefore provides support for the idea that high-resolution diffusion

[*]corresponding author: 300 Longwood Avenue, Boston, MA 02115, 857-218-4990, 617-730-0550 (fax), mukund.balasubramanian@childrens.harvard.edu.

signals, measured with the line-scan technique and receiving a boost in signal-to-noise ratio at 7T, may serve as a sensitive probe of *in vivo* laminar architecture.

Keywords

Tissue microstructure; primary somatosensory cortex (S1); tangential diffusion; primary motor cortex (M1); radial diffusion

Introduction

A key characteristic of cerebral cortex is the variation of structural properties with cortical depth—in particular, the variation of cell morphology and density (i.e., cytoarchitecture) and the variation of myelination patterns (i.e., myeloarchitecture). Since cortical areas with different cyto- or myeloarchitecture typically serve different functional roles, the ability to study the depth-dependent structure of cortex, noninvasively and *in vivo*, could provide an unprecedented opportunity to investigate structure-function relationships in the living human brain.

While MRI is an obvious candidate for noninvasive, *in vivo* studies, a major challenge for the investigation of MR signals as a function of cortical depth, often referred to as “laminar MRI” (1), lies in the fact that cortex has a thickness on the order of a couple of millimeters, not much larger than the size of the isotropic voxels typically used for *in vivo* acquisitions—on the order of a millimeter or so. As illustrated in Figure 1A, this can lead not only to partial-volume contamination from the adjacent white matter and cerebrospinal fluid (CSF), but also to the mixing of signals across different cortical layers. Substantially lowering the isotropic voxel size would reduce these partial-volume effects, but at the cost of a huge decrease in signal-to-noise ratio (SNR), which scales linearly with voxel volume. By noting, however, that structural properties in cortex vary quite rapidly in the radial direction (i.e., perpendicular to the cortical surface) but rather slowly in the tangential directions (i.e., parallel to the cortical surface), the use of a highly anisotropic voxel geometry suggests itself as a solution to this problem. As long as these anisotropic voxels are prescribed appropriately, as illustrated in Figure 1B, one receives both the benefit of high resolution in the radial direction and that of high SNR via the large voxel size in the tangential directions. As discussed later, line-scan techniques (2–4) quite naturally give rise to such anisotropic voxel geometries, making them arguably the method of choice for laminar MRI studies.

As an application of this idea, we chose to study laminar diffusion signals in human primary somatosensory cortex (S1) and primary motor cortex (M1). Previous studies consistently reported that the principal diffusion direction was mostly tangential in S1 and mostly radial in M1; the use of 1–1.5 mm (5–8) isotropic voxels in these studies is, however, of concern for the reasons given above, especially since S1 is one of the thinnest cortical areas in humans—approximately 1.5 mm in thickness (6). The goal of this study was therefore to acquire line-scan diffusion data in S1 and M1 with very high radial resolution (250–500 μm), not only in an attempt to reproduce the findings of the aforementioned studies but with reduced concerns of partial-volume effects, but also to go beyond those studies to investigate

the detailed depth dependence of the diffusion signals, and to compare these results with the known myeloarchitecture of S1 and M1 from classical histology studies (9).

Methods

Data acquisition

Eight healthy volunteers (6F/2M; ages 22–30 years), having provided informed consent under the auspices of the local institutional review board, were scanned on a Siemens 7T whole-body system (Siemens Healthineers, Erlangen, Germany) using custom-built radiofrequency (RF) coils for the head—a birdcage transmit coil and a 32-channel receive coil (10). These subjects had all participated in previous MRI studies, with their prior anatomical scans exhibiting very little head motion artifact. The whole-brain anatomical scan used in this study was a T_1-weighted dual-echo 3D MPRAGE scan (11) with FOCI adiabatic inversion pulses, acquired in ~8 minutes with the following parameters: $TE_1/TE_2/TI/TR$ = 1.8/3.7/1100/2530 ms, readout bandwidth = 651 Hz/px, FA = 7°, GRAPPA PE acceleration factor = 2 and 0.75×0.75×0.75 mm^3 voxel size (12).

The MPRAGE images, generated from the root-mean-square of the echoes, were used as an anatomical localizer for prescribing the subsequent line-scan diffusion acquisitions: the central sulcus was first identified on each hemisphere and then M1 and S1 (which lie respectively on the anterior and posterior banks of this sulcus) were inspected in search of cortical patches that were flat on the scale of a few millimeters or more. For each of the eight volunteers in this study, it was possible to find at least one such location. A single line was then prescribed, centered approximately on the central sulcus and oriented perpendicularly to M1 and S1 at this location (see Figure 2).

To address the well-known spatial nonuniformity of the B_1^+ transmit field in the adult-sized head at 7T (13,14), we employed the following calibration strategy in order to improve the accuracy of the flip angles (and thus maximize the SNR) for the line-scan diffusion acquisitions in the M1/S1 region of interest. By default, the scanner system sets the transmit reference voltage via a calibration measurement taken at isocenter, which could potentially introduce variability across subjects due to the variability in head positioning relative to isocenter. We therefore acquired a B_1^+ map (15) for each volunteer and determined the reference voltage required for the region of interest at the beginning of each experimental session. For B_0 shimming, a ~5 cm shim box was centered on the region of interest and the Siemens “3DShim” procedure was performed 2–3 times in succession prior to the diffusion scans.

For the diffusion acquisitions, we used a custom implementation of the line-scan diffusion pulse sequence first described by Chenevert et al. (16). This is a single-line technique, with the slice-select gradients for the RF excitation and refocusing pulses applied orthogonally to one another—the line is then defined by the intersection of the two slices, as shown in Figure 2A, with the excitation slice selection roughly in the axial plane and the refocusing slice selection roughly in the sagittal plane. Trapezoidal diffusion-encoding gradients were placed on either side of the crushers bracketing the refocusing pulse (see Supporting Information Figure S–1 for the pulse sequence diagram and Supporting Information Figure

S–2 for crushing considerations), making this a pulsed-gradient spin-echo (PGSE) diffusion sequence (17). The following parameters were common to all the line-scan diffusion acquisitions used in this study: TR/TE = 2000/50 ms, readout bandwidth = ~100 Hz/px, excitation/refocusing RF pulse duration = 2.0/2.5 ms with nominal FA = 90/180° and time-bandwidth product = 2.7/2.7, diffusion gradient duration/separation δ/Δ = 16.8/21.8 ms, and with the diffusion gradient amplitude G varied from 0 to 54.6 mT/m in order to achieve 21 b-values equally spaced from ~0 to 1000 s/mm^2. The voxel size along the line was either 250 or 500 μm with a 256 mm readout field of view and nominal line thickness of 3 mm, yielding voxel dimensions of either 0.25×3×3 or 0.5×3×3 mm^3.

The number of diffusion gradient directions employed was either 3 (volunteers 1–7) or 13 (volunteers 3–6, 8). For the "**3-dir**" acquisitions, the first direction was chosen to be along the line, i.e., in the radial direction of cortex for a properly prescribed line. This was approximately in the anterior/posterior (A/P) direction for the patch of M1/S1 targeted for each volunteer in this study. The other two directions were chosen to be perpendicular to the first and to one another; these two tangential directions were approximately in the medial/lateral (M/L) and superior/inferior (S/I) directions. For the 500 μm scans, a single repetition was acquired in ~2 minutes, whereas for the 250 μm scans, four repetitions were acquired (~8 minutes) in order to match the SNR of the 500 μm scans. For the "**13-dir**" data, an additional 10 diffusion gradient directions were employed, distributed approximately uniformly on the unit hemisphere. For the 500 μm scans, a single repetition was acquired in ~9 minutes; for the 250 μm scans, it was typically only possible to acquire three repetitions (~27 minutes) within each session.

Data analysis

The line-scan signals were reconstructed and analyzed offline in MATLAB (MathWorks, Natick, MA, USA), given raw multi-coil data as input. A 1D FT was applied to transform the data from k-space into physical space (i.e., the "image" domain), using the fft function in MATLAB. For the 500 μm data, where a single repetition was acquired, a root-sum-of-squares (rSoS) operation was then applied in order to combine signals across receive-coil channels. For the 250 μm data, where multiple repetitions were acquired, complex-valued signal averaging was performed prior to coil combination. Before averaging across repetitions, however, it was necessary to account for the well-known shot-to-shot (i.e., TR-to-TR) phase variations in diffusion-weighted signals (18). The following phase-correction strategy was therefore implemented, exploiting the fact that the (within-TR) phase varies somewhat slowly across space (19–21): for each voxel, the complex-valued line-scan signal was first spatially averaged over a 33-voxel window (~8 mm in extent) centered on the voxel, and the phase of this average was subtracted from the phase of the voxel. This was done not only for each voxel and TR (and hence for each diffusion gradient direction and b-value), but also on a per-channel basis, thus removing any phase offsets between coil channels. Complex-valued averaging across repetitions was then performed on the phase-corrected data (22), followed by rSoS coil combination, resulting in a signal magnitude S for each voxel, direction and b-value.

For the 3-dir data, per-voxel apparent diffusion coefficients (ADCs) were derived for each direction individually. This was done by first fitting a straight line to the logarithm of the magnitude signal ln(S) versus b-value using linear regression (regress function in MATLAB); the resulting slope and intercept were then used to initialize nonlinear fitting to a monoexponential function via the Levenberg-Marquardt algorithm (lsqnonlin function in MATLAB), yielding the final estimate of the ADC for each voxel and direction. For the 13-dir data, the above MATLAB functions were used again, but now to fit the diffusion tensor (23,24) simultaneously to signals from all diffusion gradient directions. Linear fitting of ln(S) versus b-value and direction was used to derive an initial estimate of the diffusion tensor; this linear estimate was then used to initialize the Levenberg-Marquardt algorithm, yielding the final estimate of the diffusion tensor for each voxel. In all of the fits above, only the 19 b-values from 100 to 1000 s/mm^2 were used, in order to minimize potential contamination from perfusion effects (i.e., intravoxel incoherent motion, IVIM) at low b-values (25). Two metrics were derived from the diffusion tensor: (i) the fractional anisotropy or FA (26) and (ii) the radiality index $\left|\overrightarrow{\varepsilon} \bullet \hat{n}\right|$, defined only for gray matter voxels with FA ≥ 0.05 (5,6), where $\overrightarrow{\varepsilon}$ is the principal eigenvector of the diffusion tensor and $\hat{n}$ is the unit vector normal to the cortical surface—thus a radiality index of zero is indicative of a principal diffusion direction tangential to the cortical surface, whereas a value of one indicates a radial diffusion direction, perpendicular to the cortical surface.

Results

Figure 3 shows plots of ADC versus location for the 3-dir acquisitions from volunteer 1, at 500 and 250 μm radial resolution. The following observations hold at both resolutions but are more convincing at 250 μm resolution, for which eight voxels lie within S1, versus only three voxels at 500 μm: (i) In the upper or “superficial” part of S1, the ADCs are very similar for the three directions (standard deviation: 0.02 μm^2/ms), suggestive of isotropic diffusion here. (ii) In deep S1, on the other hand, the ADCs are very different for the three directions (standard deviation: 0.24 μm^2/ms), taking on the lowest value in the radial direction (along the line, roughly in the A/P direction, and shown in red). Although the (tensor-based) principal diffusion direction cannot be determined from the use of only three diffusion gradient directions, we can at least say that this observation of non-radial diffusion is consistent with the diffusion direction being primarily tangential in deep S1. (iii) Non-radial diffusion is also seen in the white matter adjacent to S1 and M1. (iv) Non-radial diffusion is not, however, observed in deep M1, allaying concerns that the results in deep S1 may simply be due to partial voluming of the adjacent white matter. (v) In this regard, note also the steep increase in ADCs as one goes from S1 to CSF, or from M1 to CSF, with values in CSF of ~2.5 μm^2/ms (outside the range of the plots). The steepness of these curves suggests that very little partial voluming has occurred between gray matter and the adjacent CSF.

Figure 4 presents plots of signal magnitude versus b-value for both a 500 μm voxel and a 250 μm voxel in deep S1 in volunteer 1, confirming that the data are fit well with a monoexponential function, as would be expected given the b-value range of 100 to 1000 s/mm^2. Similar SNRs (of ~25) were seen in S1 and M1 at both 500 μm (one repetition) and

250 μm resolution (four repetitions), which we take as evidence of a successful strategy of phase correction and complex-valued averaging across repetitions (see Methods and Supporting Information Table S–1). Monte Carlo simulations reveal that this level of SNR results in a precision of ~10% in the estimation of ADCs (see Supporting Information Table S–2).

Figure 5 shows results from volunteers 2–7 for the 3-dir acquisitions at 250 μm radial resolution. In S1, the same overall pattern seen in volunteer 1 is also visible in each of these individuals: namely, very little evidence for anisotropy in superficial S1 and high anisotropy consistent with tangential diffusion in deep S1. We remark that this pattern can be readily appreciated without resorting to averaging across individuals or extensive averaging across different locations on the cortical sheet for a given individual.

Figure 6 shows plots of FA and radiality index versus location for volunteer 6, derived from the 13-dir acquisitions at 500 and 250 μm radial resolution. Note the rather low FA values (~0.1) in superficial S1 versus the much higher values (~0.4) in deep S1, where low values of the radiality index are seen, indicating a principal diffusion direction that is predominantly tangential. These results confirm what was qualitatively surmised from the 3-dir results above, which lacked the quantitative measures of anisotropy (i.e., FA) and directionality with respect to cortex (i.e., radiality index) now available. In M1, moderate FA values (~0.2) are seen, with high values of the radiality index at almost all cortical depths except near the boundaries, indicating a principal diffusion direction that is predominantly radial. Evidence for radial diffusion in M1 is much clearer here than in the 3-dir results, where it was somewhat harder to appreciate (see Figure 5), likely on account of M1 not having very high FA values, unlike deep S1, resulting in less striking differences in ADC across diffusion gradient directions. Similar results for FA and radiality index in M1 and S1 were obtained on the four other individuals for whom 13-dir data were acquired, as shown in Figure 7.

If we identify superficial cortical layers with the upper half of cortex and deep layers with the lower half, a statistical comparison between the two can be performed, as shown in Tables 1 and 2 for S1 and M1, respectively. Highly significant differences in FA and radiality were found for superficial versus deep S1 (Table 1), but not for superficial versus deep M1 (Table 2). While these statistics serve to reinforce the findings described in the previous paragraph, we caution against general use of the assumption that the superficial and deep layers strictly correspond to the upper and lower halves of cortex, since layer positions are known to vary with the cortical folding pattern (and possibly other factors), a point we return to in the Discussion.

Discussion

Our results are in agreement with prior *in vivo* studies reporting mostly tangential diffusion in S1 and mostly radial diffusion in M1 (5–8), but with far less concern that these observations may be attributed to partial-volume effects, given the high radial resolution (250–500 μm) used here. Going further than those studies, we show that the tangential diffusion in S1 originates from the deeper layers, with very little evidence of diffusion-tensor

anisotropy in the superficial layers. These results are also in good agreement with the myelination patterns in S1 and M1 known from histology: in S1, dense bands of tangential myelinated fibers run through the deep layers but not the superficial ones, and in M1, radial myelinated fibers are prominent at most cortical depths (see Figure 8). We remark that diffusion-weighted signals are not specific to myelinated fibers—unmyelinated axon bundles have also been shown to result in robust diffusion anisotropy (27,28) and non-axonal processes such as those from dendrites and glia are further contributors to gray matter diffusion signals (29–31). Nonetheless, the agreement between our results and histology supports the idea that high-resolution diffusion signals may serve as a sensitive probe of *in vivo* cortical myeloarchitecture.

The benefits of high resolution might suggest the investigation of laminar MRI signals via *ex vivo* studies, since the extremely long scan durations that are possible here enable the acquisition of small voxels with adequate SNR, achieved primarily through the use of extensive signal averaging. *Ex vivo* diffusion studies are challenging, however, since the fixation process can lead to a substantial reduction in both (i) T_2 (32,33), leading to a loss of signal relative to the use of the same TE *in vivo*, and (ii) ADC (32,34), requiring the use of much higher b-values than *in vivo*, which typically means a significant increase in TE to accommodate the increase in diffusion weighting, and thus a further loss of SNR. Interestingly, *ex vivo* studies of S1 have shown either an absence of tangential diffusion (35) or much less tangential diffusion than *in vivo* (6), contradicting the general belief that diffusion directionality is preserved well between *ex vivo* and *in vivo* studies. Previously, this discrepancy could perhaps have been dismissed as being due to partial voluming of the white matter adjacent to S1 in low-resolution *in vivo* data, but we see very little to suggest significant partial-volume effects in our high-resolution data, given the steep ADC transition from cortex to CSF (see Figure 3 and accompanying text) and the lack of evidence for tangential diffusion in deep M1 (see radiality index plots in Figure 6).

In the developing brain, cortex typically exhibits radial diffusion (36,37), as do the majority of cortical areas in the adult brain (6). Thus it is interesting to highlight the rare instances when this “rule” is violated, as it seems to be in deep S1. We note that the diffusion direction here appears to be approximately in the S/I direction (see Figures 3 and 5). This direction is roughly orthogonal to the head-foot axis of the somatotopic representation of the body (i.e., the “homunculus”) in S1, consistent with an interpretation of high connectivity within body part (e.g., within the somatotopic representation of the hands). This particular pattern of deep-layer connectivity likely has implications for the neural computations executed within this cortical area, the elucidation of which could ultimately lead to a better understanding of the functionality of S1 and its role in the perception of touch.

We now return to a point raised in the Introduction, namely that line-scan techniques might be the method of choice for laminar MRI studies. One apparent limitation of this technique is that it is difficult to achieve very thin lines, just as it is difficult to achieve thin slices in 2D acquisitions, since doing so while attempting to maintain slice-selection profiles typically requires the use of very long RF pulses, which are undesirable due to the possibility of significant spin relaxation effects during the pulses. However, if the line is prescribed such that it is perpendicular to the cortex in the region of interest, this limitation becomes

inconsequential since it is not just acceptable, but in fact desirable (from an SNR perspective), to have large voxel size in the tangential directions, along which cortical architecture varies quite slowly. In the radial direction, along which cortical architecture varies rather rapidly, the requirement of small voxel size is met by simply increasing the readout gradient area to a suitably high value. Thus line-scan acquisitions naturally lend themselves to the anisotropic voxel geometry best suited for laminar MRI (see Figure 1). Furthermore, by virtue of being a single-shot technique, relatively simple phase-correction schemes can be employed for line-scan diffusion acquisitions, as performed here prior to complex-valued signal averaging across repetitions (see Methods), versus the far more complicated schemes required for multi-shot methods (18,38). We also note that although the most traditional line-scan methodology involves the use of perpendicular excitation and refocusing slice-select gradients (2–4), line scanning may also be performed through the use of other techniques such as outer volume suppression (39,40), where saturation bands are added to 2D slice selection in an attempt to null signal from spins outside the desired line. Indeed, despite the difficulty of completely suppressing unwanted signal with this strategy, line-scan techniques based on outer volume suppression have found use in laminar fMRI studies of rodents in small-bore scanners (41–43).

EPI has largely superseded line scanning in modern diffusion studies, given its much higher spatial coverage per unit scan time[†]. However, even if it were feasible to acquire EPI data with comparable resolution to our line scans ($0.25\times3\times3$ mm^3) without making the TE prohibitively long, it is highly improbable that multiple lines of these EPI voxels would intersect cortical patches orthogonally—a requirement if one is to minimize partial-volume effects in laminar studies—given the substantial curvature and folding pattern of human cerebral cortex. Thus it is unclear that the increased spatial coverage provided by EPI would actually be of any real benefit for laminar MRI at high radial resolution—a point that also applies to any other Cartesian sampling/reconstruction scheme such as the use of anisotropic 3D FLASH voxels for laminar fMRI (46) or even the use of multiple, parallel lines within the line-scan framework (47–49). One could, however, envision an extension of our approach employing multiple, non-parallel lines, with each line independently prescribed with respect to a separate patch of cortex. This could substantially increase the efficiency of our acquisition scheme, but would likely require considerable offline planning on a previously-acquired anatomical scan, with care taken to avoid having any lines intersect at a location of interest, disrupting the magnetization there. Moreover, incidental magnetization transfer effects (50–52) would also have to be assessed.

Field strengths of 7T and above are not necessarily seen as being advantageous for *in vivo* diffusion MRI of the human brain from an SNR perspective, given the combination of shorter T_2 values at higher field and the long TEs typical of EPI-based diffusion acquisitions (53). These long TEs result not only from the time required to accommodate diffusion-encoding gradients, but also from the time required for the EPI readout. The readout time for

[†]Historically, line-scan imaging has found use in clinical diffusion studies (44) due to its modest gradient hardware requirements and resistance to the distortions and artifacts often associated with EPI. Over time, however, advances in gradient performance, acquisition strategies and image reconstruction have made EPI more practical and effective, providing whole-brain coverage 4–6 times faster than a comparable line-scan acquisition (45). As a result, EPI has supplanted line-scan imaging for most diffusion MRI applications. Nevertheless, line-scan techniques still typically allow higher spatial resolution along the readout direction.

a comparable line-scan acquisition can be considerably shorter, however, allowing a substantial reduction in TE for the same diffusion encoding. For the 50 ms TE (and 2 s TR) used here, we estimate a doubling of SNR at 7T versus 3T, based on the simulations of Uğurbil et al. (see ref. #54, Figure 20). This can be translated into a doubling of the radial resolution per unit scan time at 7T versus 3T, for a fixed SNR. These simulations assume similar gradient and RF coil performance at the two field strengths, however—an assumption that may not hold in practice.

The laminar diffusion patterns observed in this study were consistent across subjects and were conspicuous without averaging data across different locations on the cortical sheet—a common practice in studies of the cortical depth dependence of MR signals (55,56). This practice can be problematic, however, since layer positions are known to vary with the cortical folding pattern, with the granular layer shifted towards the pia mater in gyral crowns and towards the white matter (i.e., in the opposite direction) in sulcal fundi (57); averaging across cortical locations could therefore lead to the undesired mixing of signals across layers. Even after accounting for this shift (58), Hinds et al. (59) have reported a systematic, residual variation in the depth of the stria of Gennari in human V1 in the direction of the eccentricity coordinate of the retinotopic representation (roughly the anterior-to-posterior direction). This suggests that factors other than cortical folding may influence the positions of layers, complicating the prediction of the layer positions from cortical geometry alone. By avoiding averaging across cortical locations, the above issues—which are not only rather complicated but also not fully understood—can be sidestepped.

The astute reader may have noticed that, with the 250 μm results in hand, one can often go back and look at the 500 μm results and identify many of the features seen in the higher-resolution data. Why then should one go through all the effort needed to acquire the higher-resolution data? The problem here is the implicit expectation that an anatomical feature will go from being barely visible at 500 μm to clearly visible at 250 μm—a rather unrealistic expectation even for a two-fold improvement in resolution. In our opinion, the true benefit of going to higher resolution comes not from the sudden appearance of a feature, but rather from an increased confidence that the observed feature is real and not attributable to the various sources of noise or artifact inherent to MR data. In our case, if we just had data at 500 μm radial resolution, where only about three data points lie clearly within S1 in volunteer 1 (see Figure 3) and volunteer 6 (see Figure 6), it is not clear how confidently we could have made statements regarding the depth dependence of diffusion signals in this cortical area; at 250 μm radial resolution, we lacked no such confidence. Indeed, one wonders if there are other, perhaps quite subtle, features in our 250 μm data that we are failing to appreciate as being real without the benefit of data with 125 μm radial resolution.

Subject motion can of course be a concern for any *in vivo*, high-resolution scans with restricted field of view, such as the line-scan acquisitions described here. For the present study, our strategy with regard to head motion was simply to recruit experienced volunteers whose prior scans had shown very little motion artifact. A strategy such as this, while feasible for preliminary investigations (see also Supporting Information Figure S–3), is obviously quite restrictive and limits the ability to draw upon volunteers from the population at large. It is our hope that techniques for prospective motion correction (60), such as those

using external trackers (61–63) or MR-based navigators (64,65), will ultimately prove useful in this setting.

In this study, we did not use b-values above 1000 s/mm^2, keeping us in the regime of validity for both monoexponential fits of signal versus b-value and diffusion-tensor fits of signal versus b-value and diffusion gradient direction. At higher b-values, kurtosis (66,67) or biexponential (68,69) signal models may be more appropriate and the laminar variation of quantities derived from fits to these models would likely be of interest, if such data could be acquired with adequate SNR. Increasing the number of diffusion gradient directions to thirty or more would also enable the measurement of orientation distribution functions (ODFs) with more angular detail than that provided by the single tensor model, e.g., via the use of spherical deconvolution (70) or persistent angular structure (PAS) algorithms (71). This additional detail comes at the cost of increased scan time, but may help clarify the situation in places where radial and tangential fibers cross and are in equal abundance, as may be the case in superficial S1, where we observed very low diffusion-tensor anisotropy. The signal models, or representations (72), above stand in contrast to biophysical models, which explicitly reference some specific aspect of tissue microstructure, e.g., axon diameter in the AxCaliber framework (73). However, any potential increase in specificity often comes at the expense of sensitivity.

Although the argument for anisotropic voxel geometry was made with cortical gray matter in mind, similar considerations may also hold for superficial white matter, which lies immediately below the cortical surface. Inspection of Figures 6 and 7 reveals consistently higher FA values for the white matter adjacent to S1 compared to the white matter adjacent to M1, perhaps reflecting differences in the ratio of tangential U-fibers (74) to radial fibers entering or exiting cortex. Again, the high-angular-resolution methods referenced in the previous paragraph may be required in order to better understand the fiber crossings here.

In closing, we have demonstrated the utility of line-scan acquisitions for investigating the depth dependence of *in vivo* diffusion signals in human cerebral cortex. Although our focus was on S1 and M1, this technique could be applied to any cortical area containing a sufficiently flat patch, and perhaps to the adjacent white matter as well. The method could also be modified to be sensitive to other MR contrast mechanisms such as longitudinal or transverse relaxation, e.g., through the use of multiple TRs or TEs to enable the measurement of laminar T_1 or T_2 values, respectively. Given the sensitivity of these relaxometry measures to myelin and iron content, combining them with diffusion-based metrics may ultimately provide a more complete MR-based description of laminar architecture, which could aid the noninvasive delineation of cortical layers and areas (75,76). The ability to study the internal structure of cortex in the living human brain would also open up opportunities to study changes over time, due to development, plasticity or aging, in health or in disease.

Supplementary Material

Refer to Web version on PubMed Central for supplementary material.

Acknowledgments

The authors would like to thank Nina Fultz and Ned Ohringer for their assistance with volunteer recruitment and data acquisition, and Itamar Ronen and Bob Turner for their helpful feedback. This work was supported by a BWH-MGH 7T Pilot Study Grant, NIH grants P41-EB015896, R01-EB019437, R01-MH111419 (*BRAIN Initiative*), R01-EB010195, R01-CA154834 and U01-EB026996 (*BRAIN Initiative*), the Athinoula A. Martinos Center for Biomedical Imaging, and the Radiology Departments at BCH, BWH and MGH, and made possible by the resources provided by NIH Shared Instrumentation Grant S10-RR019371.

References

1. Norris DG, Polimeni JR. Laminar (f)MRI: A short history and future prospects. NeuroImage 2019;197:643–649. [PubMed: 31059800]
2. Mansfield P, Maudsley AA. Line scan proton spin imaging in biological structures by NMR. Phys Med Biol 1976;21:847–852. [PubMed: 967931]
3. Maudsley AA. Multiple-line-scanning spin density imaging. J Magn Reson 1980;41:112–126.
4. Crooks LE. Selective irradiation line scan techniques for NMR imaging. IEEE Trans Nucl Sci 1980;27:1239–1244.
5. Anwander A, Pampel A, Knösche TR. In vivo measurement of cortical anisotropy by diffusion-weighted imaging correlates with cortex type. Proc Intl Soc Mag Reson Med 2010;18:109.
6. McNab JA, Polimeni JR, Wang R, Augustinack JC, Fujimoto K, Stevens A, Janssens T, Farivar R, Folkerth RD, Vanduffel W. Surface based analysis of diffusion orientation for identifying architectonic domains in the in vivo human cortex. NeuroImage 2013;69:87–100. [PubMed: 23247190]
7. Gulban OF, De Martino F, Vu AT, Yacoub E, Uğurbil K, Lenglet C. Cortical fibers orientation mapping using in-vivo whole brain 7 T diffusion MRI. NeuroImage 2018;178:104–118. [PubMed: 29753105]
8. Calamante F, Jeurissen B, Smith RE, Tournier J-D, Connelly A. The role of whole-brain diffusion MRI as a tool for studying human in vivo cortical segregation based on a measure of neurite density. Magn Reson Med 2018;79:2738–2744. [PubMed: 28921634]
9. Vogt C, Vogt O. Allgemeinere ergebnisse unserer hirnforschung. J Psychol Neurol (Leipz) 1919;25:279–462.
10. Keil B, Triantafyllou C, Hamm M, Wald LL. Design optimization of a 32-channel head coil at 7T. Proc Intl Soc Mag Reson Med 2010;18:1493.
11. van der Kouwe AJW, Benner T, Salat DH, Fischl B. Brain morphometry with multiecho MPRAGE. NeuroImage 2008;40:559–569. [PubMed: 18242102]
12. Zaretskaya N, Fischl B, Reuter M, Renvall V, Polimeni JR. Advantages of cortical surface reconstruction using submillimeter 7 T MEMPRAGE. NeuroImage 2018;165:11–26. [PubMed: 28970143]
13. Collins CM, Smith MB. Signal-to-noise ratio and absorbed power as functions of main magnetic field strength, and definition of “90°” RF pulse for the head in the birdcage coil. Magn Reson Med 2001;45:684–691. [PubMed: 11283997]
14. Vaughan JT, Garwood M, Collins CM et al. 7T vs. 4T: RF power, homogeneity, and signal-to-noise comparison in head images. Magn Reson Med 2001;46:24–30. [PubMed: 11443707]
15. Yarnykh VL. Actual flip-angle imaging in the pulsed steady state: a method for rapid three-dimensional mapping of the transmitted radiofrequency field. Magn Reson Med 2007;57:192–200. [PubMed: 17191242]
16. Chenevert TL, Pipe JG, Williams DM, Brunberg JA. Quantitative measurement of tissue perfusion and diffusion in vivo. Magn Reson Med 1991;17:197–212. [PubMed: 2067394]
17. Stejskal EO, Tanner JE. Spin diffusion measurements: spin echoes in the presence of a time-dependent field gradient. J Chem Phys 1965;42:288–292.
18. Bammer R, Holdsworth SJ, Aksoy M, Skare S. Phase Errors in Diffusion-Weighted Imaging. In: Jones DK, editor. Diffusion MRI: Theory, Methods, and Applications: New York: Oxford University Press; 2010. p 218–249.

19. Pipe JG, Farthing VG, Forbes KP. Multishot diffusion-weighted FSE using PROPELLER MRI. Magn Reson Med 2002;47:42–52. [PubMed: 11754441]
20. Prah DE, Paulson ES, Nencka AS, Schmainda KM. A simple method for rectified noise floor suppression: phase-corrected real data reconstruction with application to diffusion-weighted imaging. Magn Reson Med 2010;64:418–429. [PubMed: 20665786]
21. Holdsworth SJ, Aksoy M, Newbould RD, Yeom K, Van AT, Ooi MB, Barnes PD, Bammer R, Skare S. Diffusion tensor imaging (DTI) with retrospective motion correction for large-scale pediatric imaging. J Magn Reson Imaging 2012;36:961–971. [PubMed: 22689498]
22. Newbould RD, Skare S, Bammer R. On the utility of complex-averaged diffusion-weighted images. Proc Intl Soc Mag Reson Med 2008;16:1810.
23. Basser PJ, Mattiello J, LeBihan D. Estimation of the effective self-diffusion tensor from the NMR spin echo. J Magn Reson B 1994;103:247–254. [PubMed: 8019776]
24. Basser PJ, Mattiello J, LeBihan D. MR diffusion tensor spectroscopy and imaging. Biophys J 1994;66:259–267. [PubMed: 8130344]
25. Le Bihan D What can we see with IVIM MRI? NeuroImage 2019;187:56–67. [PubMed: 29277647]
26. Basser PJ, Pierpaoli C. Microstructural and physiological features of tissues elucidated by quantitative-diffusion-tensor MRI. J Magn Reson B 1996;111:209–219. [PubMed: 8661285]
27. Neil JJ, Shiran SI, McKinstry RC, Schefft GL, Snyder AZ, Almli CR, Akbudak E, Aronovitz JA, Miller JP, Lee BC. Normal brain in human newborns: apparent diffusion coefficient and diffusion anisotropy measured by using diffusion tensor MR imaging. Radiology 1998;209:57–66. [PubMed: 9769812]
28. Beaulieu C The basis of anisotropic water diffusion in the nervous system—a technical review. NMR Biomed 2002;15:435–455. [PubMed: 12489094]
29. Jespersen SN, Kroenke CD, Østergaard L, Ackerman JJH, Yablonskiy DA. Modeling dendrite density from magnetic resonance diffusion measurements. NeuroImage 2007;34:1473–1486. [PubMed: 17188901]
30. Budde MD, Annese J. Quantification of anisotropy and fiber orientation in human brain histological sections. Front Integr Neurosci 2013;7:3. [PubMed: 23378830]
31. Kroenke CD. Using diffusion anisotropy to study cerebral cortical gray matter development. J Magn Reson 2018;292:106–116. [PubMed: 29705039]
32. Roebroeck A, Miller KL, Aggarwal M. Ex vivo diffusion MRI of the human brain: Technical challenges and recent advances. NMR Biomed 2019;32:e3941. [PubMed: 29863793]
33. Shepherd TM, Thelwall PE, Stanisz GJ, Blackband SJ. Aldehyde fixative solutions alter the water relaxation and diffusion properties of nervous tissue. Magn Reson Med 2009;62:26–34. [PubMed: 19353660]
34. D'Arceuil HE, Westmoreland S, de Crespigny AJ. An approach to high resolution diffusion tensor imaging in fixed primate brain. NeuroImage 2007;35:553–565. [PubMed: 17292630]
35. Aggarwal M, Nauen DW, Troncoso JC, Mori S. Probing region-specific microstructure of human cortical areas using high angular and spatial resolution diffusion MRI. NeuroImage 2015;105:198–207. [PubMed: 25449747]
36. McKinstry RC, Mathur A, Miller JH, Ozcan A, Snyder AZ, Schefft GL, Almli CR, Shiran SI, Conturo TE, Neil JJ. Radial organization of developing preterm human cerebral cortex revealed by non-invasive water diffusion anisotropy MRI. Cereb cortex 2002;12:1237–1243. [PubMed: 12427675]
37. Kroenke CD, Van Essen DC, Inder TE, Rees S, Bretthorst GL, Neil JJ. Microstructural changes of the baboon cerebral cortex during gestational development reflected in magnetic resonance imaging diffusion anisotropy. J Neurosci 2007;27:12506–12515. [PubMed: 18003829]
38. Pipe JG. Non-EPI Pulse Sequences for Diffusion MRI. In: Jones DK, editor. Diffusion MRI: Theory, Methods, and Applications: New York: Oxford University Press; 2010. p 218–249.
39. Le Roux P, Gilles RJ, McKinnon GC, Carlier PG. Optimized outer volume suppression for single-shot fast spin-echo cardiac imaging. J Magn Reson Imaging 1998;8:1022–1032. [PubMed: 9786138]

40. Wargo CJ, Gore JC. Localized high-resolution DTI of the human midbrain using single-shot EPI, parallel imaging, and outer-volume suppression at 7 T. Magn Reson Imaging 2013;31:810–819. [PubMed: 23541390]
41. Yu X, Qian C, Chen D-y, Dodd SJ, Koretsky AP. Deciphering laminar-specific neural inputs with line-scanning fMRI. Nat Methods 2014;11:55–58. [PubMed: 24240320]
42. Albers F, Schmid F, Wachsmuth L, Faber C. Line scanning fMRI reveals earlier onset of optogenetically evoked BOLD response in rat somatosensory cortex as compared to sensory stimulation. NeuroImage 2018;164:144–154. [PubMed: 28012967]
43. Nunes D, Shemesh N. Line-scanning diffusion fMRI reveals a rapid-onset (<200 ms) component. Proc Intl Soc Mag Reson Med 2019;27:1056.
44. Hüppi PS, Maier SE, Peled S, Zientara GP, Barnes PD, Jolesz FA, Volpe JJ. Microstructural development of human newborn cerebral white matter assessed in vivo by diffusion tensor magnetic resonance imaging. Pediatr Res 1998;44:584. [PubMed: 9773850]
45. Kubicki M, Maier SE, Westin C-F, Mamata H, Ersner-Hershfield H, Estepar R, Kikinis R, Jolesz FA, McCarley RW, Shenton ME. Comparison of single-shot echo-planar and line scan protocols for diffusion tensor imaging. Acad Radiol 2004;11:224–232. [PubMed: 14974598]
46. Kashyap S, Ivanov D, Havlicek M, Sengupta S, Poser BA, Uludağ K. Resolving laminar activation in human V1 using ultra-high spatial resolution fMRI at 7T. Sci Rep 2018;8:17063. [PubMed: 30459391]
47. Ailion DC, Ganesan K, Case TA, Christman RA. Rapid line scan technique for artifact-free images of moving objects. Magn Reson Imaging 1992;10:747–754. [PubMed: 1461068]
48. Gudbjartsson H, Maier SE, Mulkern RV, Mórocz IÁ, Patz S, Jolesz FA. Line scan diffusion imaging. Magn Reson Med 1996;36:509–519. [PubMed: 8892201]
49. Maier SE, Gudbjartsson H, Patz S, Hsu L, Lovblad KO, Edelman RR, Warach S, Jolesz FA. Line scan diffusion imaging: characterization in healthy subjects and stroke patients. AJR Am J Roentgenol 1998;171:85–93. [PubMed: 9648769]
50. Dixon WT, Engels H, Castillo M, Sardashti M. Incidental magnetization transfer contrast in standard multislice imaging. Magn Reson Imaging 1990;8:417–422. [PubMed: 2392030]
51. Melki PS, Mulkern RV. Magnetization transfer effects in multislice RARE sequences. Magn Reson Med 1992;24:189–195. [PubMed: 1556927]
52. Constable RT, Anderson AW, Zhong J, Gore JC. Factors influencing contrast in fast spin-echo MR imaging. Magn Reson Imaging 1992;10:497–511. [PubMed: 1501520]
53. Gallichan D Diffusion MRI of the human brain at ultra-high field (UHF): A review. NeuroImage 2018;168:172–180. [PubMed: 28428047]
54. Uğurbil K, Xu J, Auerbach EJ et al. Pushing spatial and temporal resolution for functional and diffusion MRI in the Human Connectome Project. NeuroImage 2013;80:80–104. [PubMed: 23702417]
55. Koopmans PJ, Barth M, Orzada S, Norris DG. Multi-echo fMRI of the cortical laminae in humans at 7 T. NeuroImage 2011;56:1276–1285. [PubMed: 21338697]
56. Marques JP, Khabipova D, Gruetter R. Studying cyto and myeloarchitecture of the human cortex at ultra-high field with quantitative imaging: R1, R2* and magnetic susceptibility. NeuroImage 2017;147:152–163. [PubMed: 27939794]
57. Bok ST. Der Einfluß der in den Furchen und Windungen auftretenden Krümmungen der Großhirnrinde auf die Rindenarchitektur. Z Gesamte Neurol Psychiatr 1929;121:682–750.
58. Waehnert MD, Dinse J, Weiss M, Streicher MN, Waehnert P, Geyer S, Turner R, Bazin P-L. Anatomically motivated modeling of cortical laminae. NeuroImage 2014;93:210–220. [PubMed: 23603284]
59. Hinds O, Balasubramanian M, Augustinack JC, Schwartz EL, Fischl B, Polimeni JR. Variation in cortical depth of the stria of Gennari seen in high-resolution ex vivo MRI of human V1. 21st Annu Meet Organ Hum Brain Mapp 2015;21:WT4084.
60. Maclaren J, Herbst M, Speck O, Zaitsev M. Prospective motion correction in brain imaging: a review. Magn Reson Med 2013;69:621–636. [PubMed: 22570274]

61. Zaitsev M, Dold C, Sakas G, Hennig J, Speck O. Magnetic resonance imaging of freely moving objects: prospective real-time motion correction using an external optical motion tracking system. NeuroImage 2006;31:1038–1050. [PubMed: 16600642]
62. Frost R, Wighton P, Karahanoğlu FI, Robertson RL, Grant PE, Fischl B, Tisdall MD, van der Kouwe AJW. Markerless high-frequency prospective motion correction for neuroanatomical MRI. Magn Reson Med 2019;82:126–144. [PubMed: 30821010]
63. Ooi MB, Aksoy M, Maclaren J, Watkins RD, Bammer R. Prospective motion correction using inductively coupled wireless RF coils. Magn Reson Med 2013;70:639–647. [PubMed: 23813444]
64. Tisdall MD, Hess AT, Reuter M, Meintjes EM, Fischl B, van der Kouwe AJW. Volumetric navigators for prospective motion correction and selective reacquisition in neuroanatomical MRI. Magn Reson Med 2012;68:389–399. [PubMed: 22213578]
65. Wallace TE, Afacan O, Waszak M, Kober T, Warfield SK. Head motion measurement and correction using FID navigators. Magn Reson Med 2019;81:258–274. [PubMed: 30058216]
66. Jensen JH, Helpern JA, Ramani A, Lu H, Kaczynski K. Diffusional kurtosis imaging: the quantification of non-Gaussian water diffusion by means of magnetic resonance imaging. Magn Reson Med 2005;53:1432–1440. [PubMed: 15906300]
67. Jensen JH, Helpern JA. MRI quantification of non-Gaussian water diffusion by kurtosis analysis. NMR Biomed 2010;23:698–710. [PubMed: 20632416]
68. Mulkern RV, Gudbjartsson H, Westin CF, Zengingonul HP, Gartner W, Guttmann CRG, Robertson RL, Kyriakos W, Schwartz R, Holtzman D. Multi-component apparent diffusion coefficients in human brain. NMR Biomed 1999;12:51–62. [PubMed: 10195330]
69. Maier SE, Mulkern RV. Biexponential analysis of diffusion-related signal decay in normal human cortical and deep gray matter. Magn Reson Imaging 2008;26:897–904. [PubMed: 18467062]
70. Tournier J-D, Calamante F, Connelly A. Robust determination of the fibre orientation distribution in diffusion MRI: non-negativity constrained super-resolved spherical deconvolution. NeuroImage 2007;35:1459–1472. [PubMed: 17379540]
71. Jansons KM, Alexander DC. Persistent angular structure: new insights from diffusion magnetic resonance imaging data. Inverse Probl 2003;19:1031–1046.
72. Novikov DS, Kiselev VG, Jespersen SN. On modeling. Magn Reson Med 2018;79:3172–3193. [PubMed: 29493816]
73. Assaf Y, Blumenfeld-Katzir T, Yovel Y, Basser PJ. AxCaliber: a method for measuring axon diameter distribution from diffusion MRI. Magn Reson Med 2008;59:1347–1354. [PubMed: 18506799]
74. Gray H, Lewis WH. Anatomy of the human body, 20th edition. Philadelphia and New York, Lea & Febiger 1918.
75. Ganepola T, Nagy Z, Ghosh A, Papadopoulo T, Alexander DC, Sereno MI. Using diffusion MRI to discriminate areas of cortical grey matter. NeuroImage 2018;182:456–468. [PubMed: 29274501]
76. Trampel R, Bazin P-L, Pine K, Weiskopf N. In-vivo magnetic resonance imaging (MRI) of laminae in the human cortex. NeuroImage 2019;197:707–715. [PubMed: 28942063]
77. Hubel DH. Eye, brain, and vision: Scientific American Library/Scientific American Books; 1995.

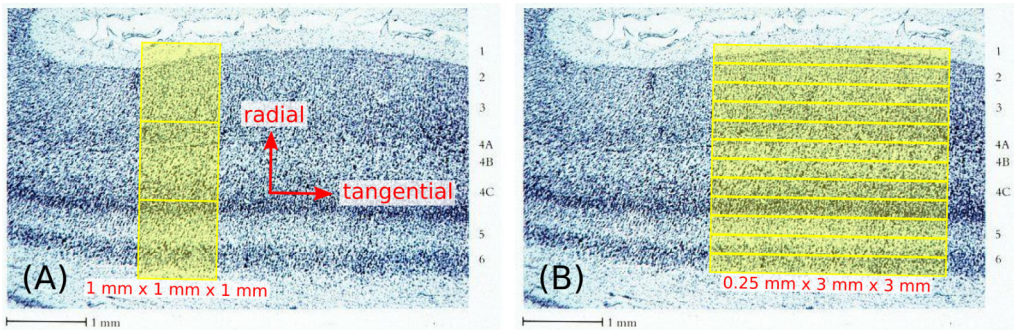

FIG. 1.

Nissl stain of primary visual cortex (reproduced from ref. #77), illustrating the cytoarchitecture of cortical gray matter. The use of 1 mm isotropic voxels shown in (A) inevitably leads to substantial mixing of signals from different cortical layers, as well as a high likelihood of partial-volume contamination from the adjacent white matter and CSF. On the other hand, the use of highly anisotropic voxels, as shown in (B) for the example of 0.25×3×3 mm voxels, can greatly reduce these partial-volume effects without sacrificing SNR, as long as the voxels are suitably positioned and oriented with respect to the radial and tangential directions of the cortical surface, indicated in (A). Although the points above are illustrated on primary visual cortex (V1) in this figure, they are applicable to any cortical area, e.g., primary somatosensory cortex (S1) and primary motor cortex (M1), which are the focus of this study.

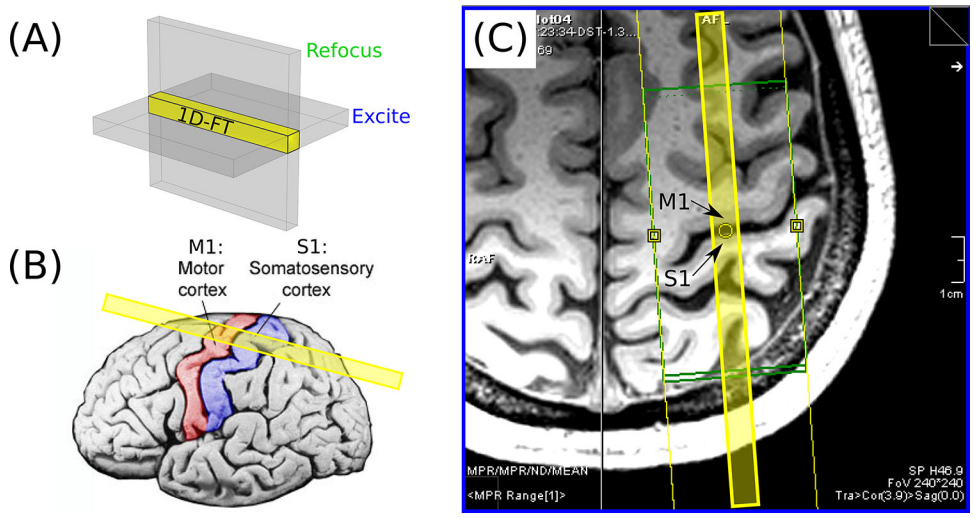

FIG. 2.

(A) An illustration of the concept underlying the spin-echo line-scan technique (2–4): by applying the slice-select gradients for the RF excitation and refocusing pulses orthogonally to one another, the MR signal arises from the column of spins within the intersection of the two slices, shown in yellow. This “line” only requires Fourier encoding in one direction and can thus be reconstructed via a 1D Fourier Transform (FT), with no need for phase encoding. (B) The prescription of the line shown with respect to a surface rendering of cortex, with M1 and S1 colored red and blue, respectively. (C) A slice through the 3D MPRAGE data of volunteer 1, as seen on the scanner console. Note the relatively flat patch of M1 and S1 adjacent to the yellow circle; the line (shown in yellow overlay) was prescribed to be as perpendicular as possible to cortex at this location.

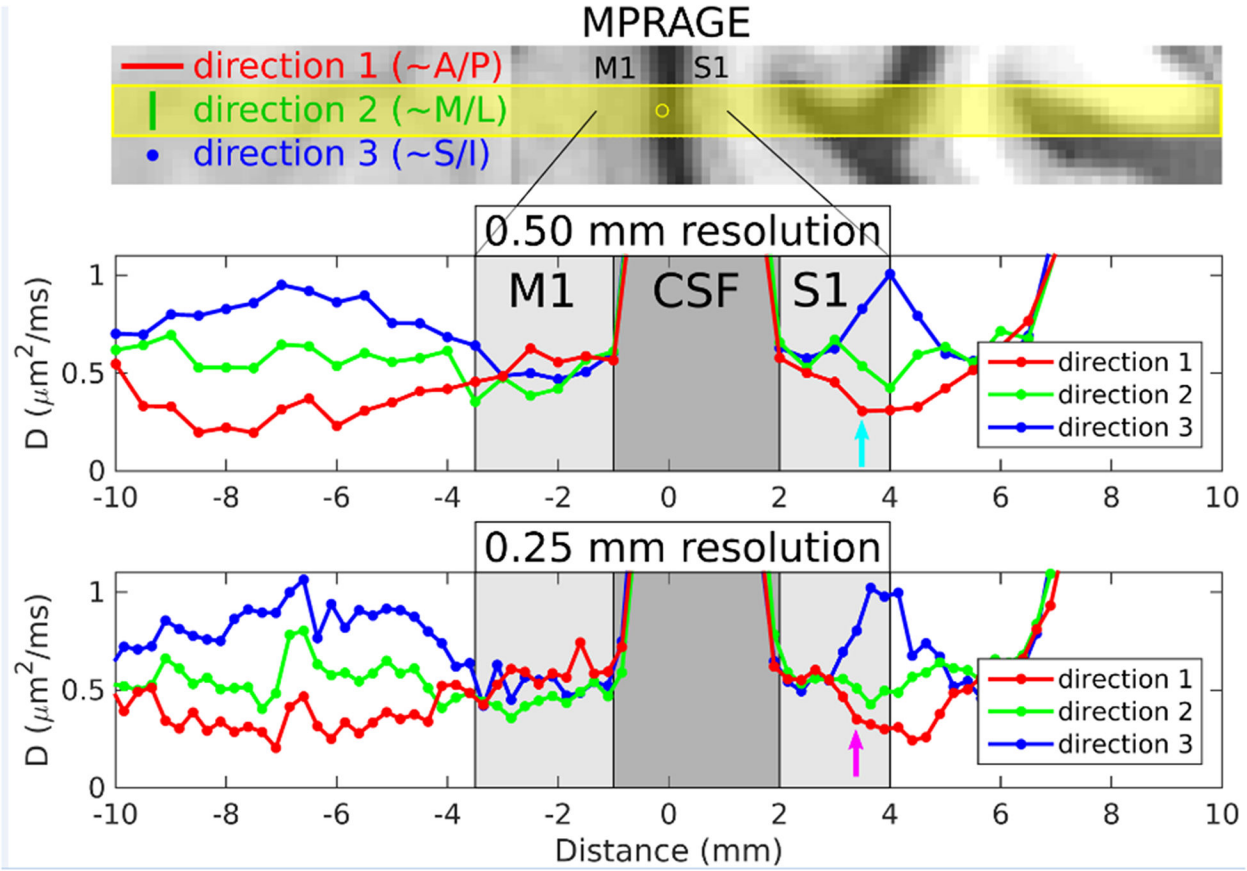

FIG. 3.

Results from volunteer 1 for the 3-dir acquisitions at 500 and 250 μm radial resolution. The top panel shows MPRAGE data resampled into the same orientation as the line-scan acquisitions. The prescribed line location and thickness are overlaid in yellow, with the yellow circle indicating the center point of the line (i.e., the origin in the plots below). For the three directions indicated (direction 1: ~A/P=anterior/posterior and radial to M1/S1 at this location, direction 2: ~M/L=medial/lateral and tangential to M1/S1 at this location, direction 3: ~S/I=superior/inferior and also tangential to M1/S1 at this location), plots of apparent diffusion coefficient D versus position along the line are shown in the middle and bottom panels for the 500 and 250 μm radial resolution acquisitions, respectively. M1 and S1 (light gray shaded regions) and central sulcus CSF (dark gray shaded region) were delineated based on the MPRAGE image in the top panel.

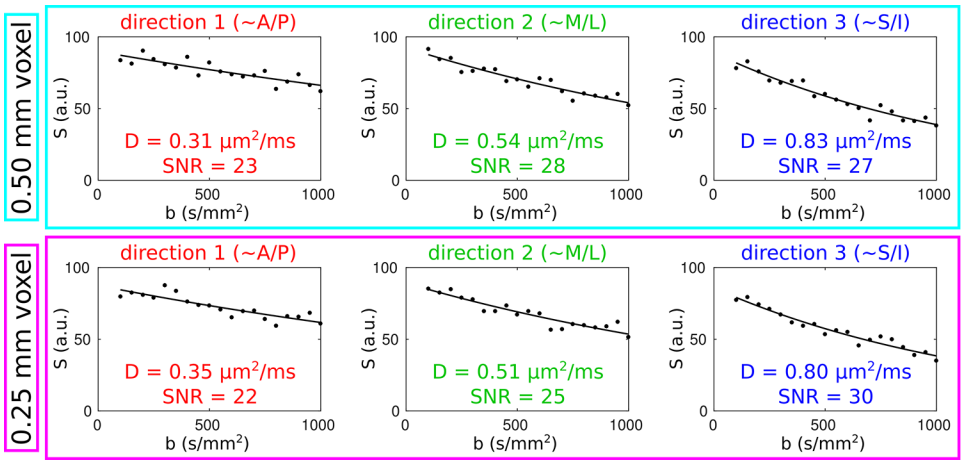

FIG. 4.

For the 500 μm voxel (in deep S1) indicated by the cyan arrow in Figure 3, the upper panel shows plots of signal magnitude versus b-value for each of the directions in the 3-dir acquisitions (dots=data points, curves=monoexponential fits) and the lower panel shows the corresponding plots for the 250 μm voxel indicated by the purple arrow in Figure 3. Along with the apparent diffusion coefficients D derived from the fits, SNR estimates are also shown; these were calculated by dividing the y-intercept of the fitted curves by the standard deviation of the residuals.

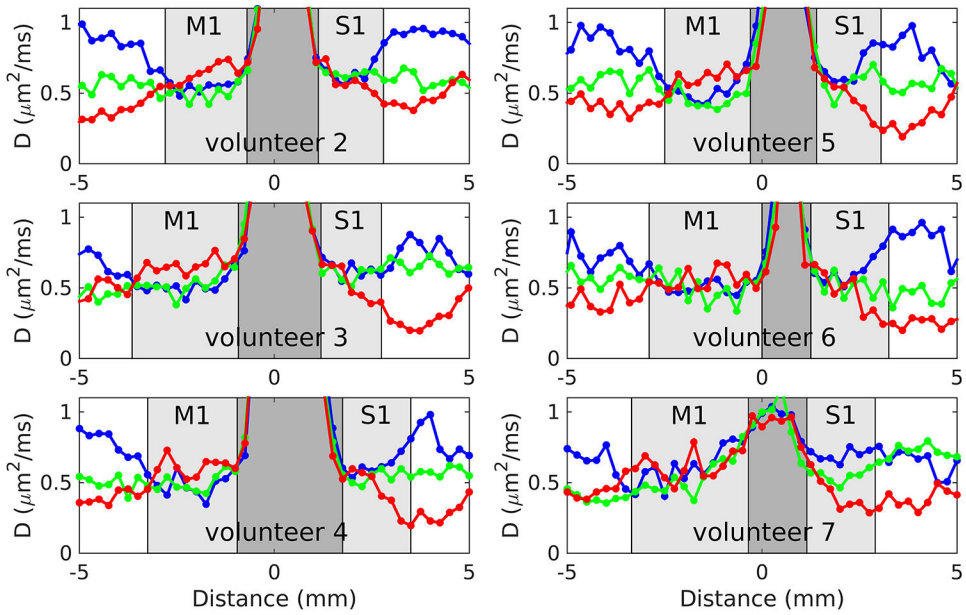

FIG. 5.

Plots of ADC versus location for volunteers 2–7, for the 3-dir acquisitions at 250 μm radial resolution. As in Figure 3, the red curves correspond to the diffusion gradient direction being in the radial direction, along the line and in roughly the A/P direction, whereas the green and blue curves correspond to two orthogonal diffusion gradient directions, tangent to cortex, in roughly the M/L and S/I directions, respectively.

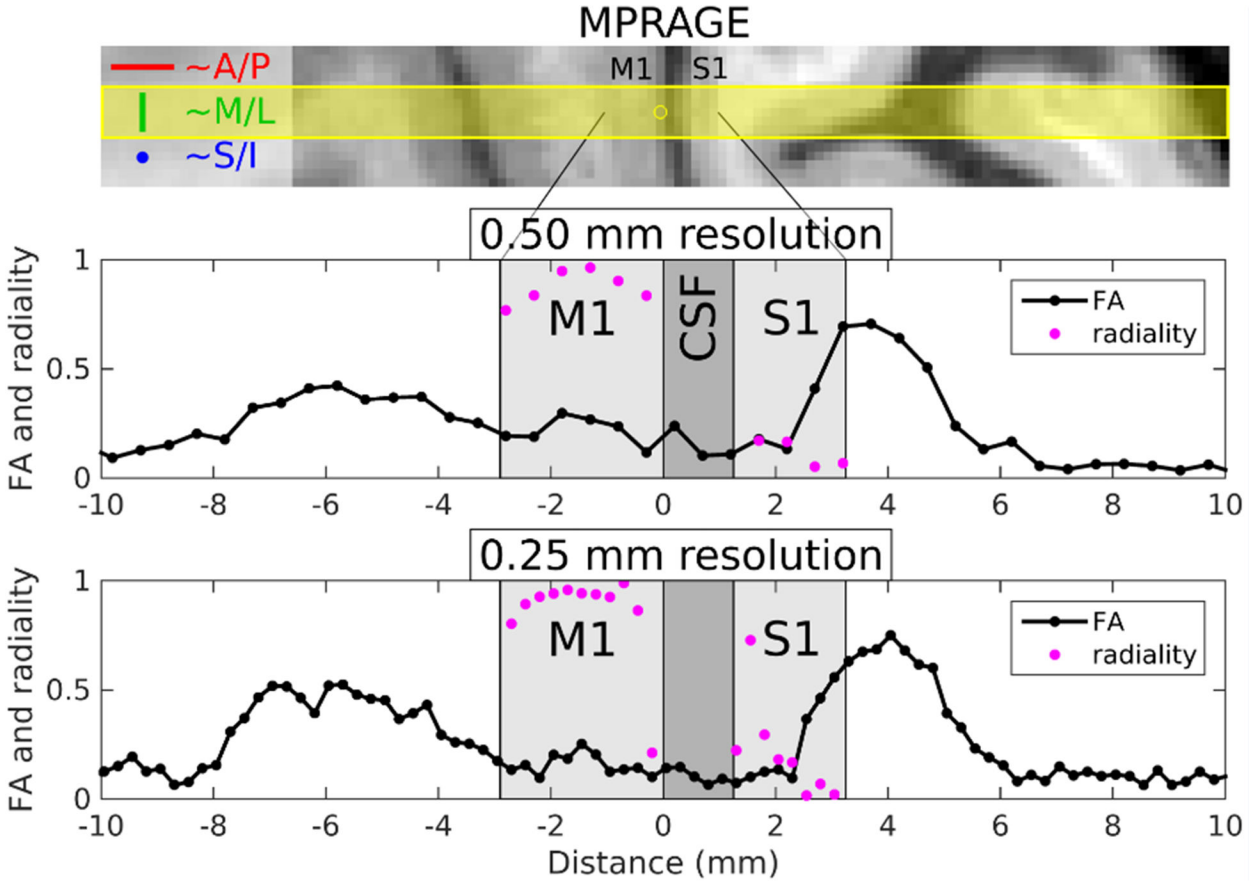

FIG. 6.

Results from volunteer 6 for the 13-dir acquisitions at 500 and 250 μm radial resolution. The top panel shows MPRAGE data resampled into the same orientation as the line-scan acquisitions, with the prescribed line overlaid in yellow and the yellow circle indicating the origin in the plots below. Plots of FA and radiality index versus position along the line are shown in black and purple, respectively, for the 500 μm (middle panel) and 250 μm (bottom panel) acquisitions. Note that the radiality index is only defined for gray matter voxels with FA ≥ 0.05.

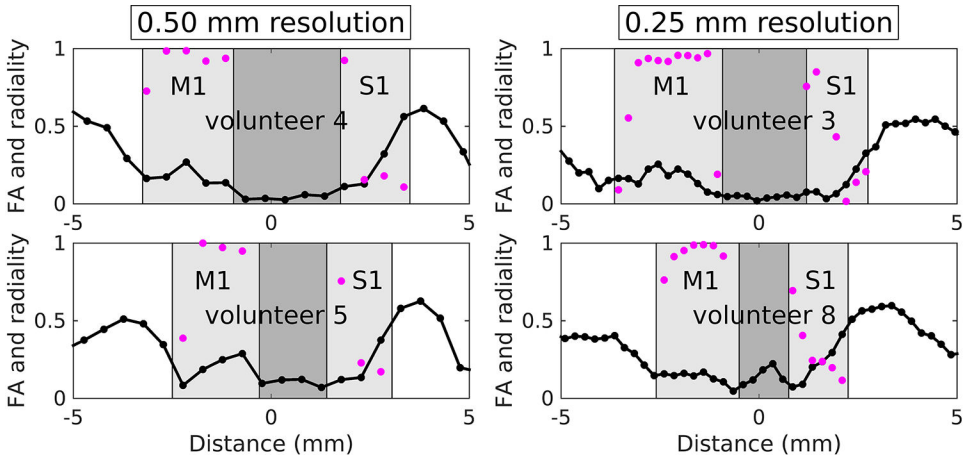

FIG. 7.

Plots of FA (black) and radiality index (purple) versus location, derived from the 13-dir acquisitions, for volunteers 4 and 5 (500 μm radial resolution) and volunteers 3 and 8 (250 μm radial resolution).

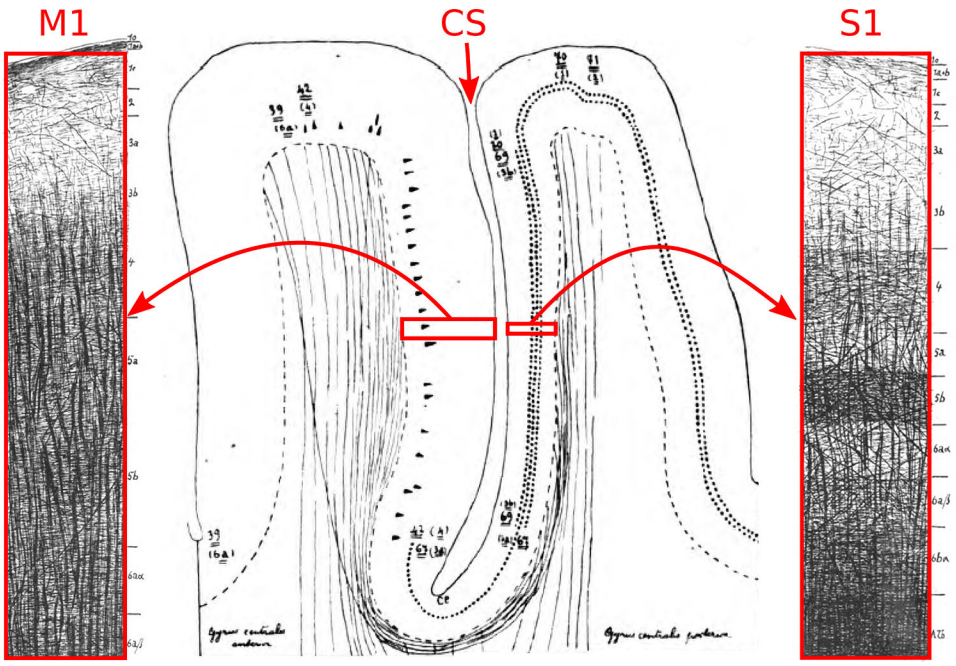

FIG. 8.

Myeloarchitecture of M1 and S1, adapted from the seminal monograph of Vogt and Vogt (9). In M1, note the dominance of radial myelinated fibers at most cortical depths, and in S1, note the pronounced tangential myelinated fibers in the deep layers. CS=central sulcus.

TABLE 1.

Mean ± standard deviation of FA and radiality for superficial and deep S1 along with the p-values resulting from t-test comparisons of superficial versus deep FA and radiality. Data are from all 13-dir acquisitions at 500 and 250 μm radial resolution (volunteers 3–6 and 8).

	FA	radiality
superficial S1	0.11 ± 0.04	0.45 ± 0.28
deep S1	0.36 ± 0.16	0.12 ± 0.07
p-value	< 0.001	< 0.001

TABLE 2.

Mean ± standard deviation of FA and radiality for superficial and deep M1 along with the p-values resulting from t-test comparisons of superficial versus deep FA and radiality. Data are from all 13-dir acquisitions at 500 and 250 μm radial resolution (volunteers 3–6 and 8).

	FA	radiality
superficial M1	0.16 ± 0.06	0.87 ± 0.23
deep M1	0.17 ± 0.05	0.82 ± 0.23
p-value	0.56	0.52